TITLE: Kinetic and static analysis of poly-(adenosine diphosphate-ribose) polymerase-1 (PARP-1) targeted ^{18}F-FluorThanatrace (^{18}F-FTT) PET images of ovarian cancer

Author list: Anthony J. Young, BS[1], Austin R. Pantel, MD, MSTR[1], Varsha Viswanath, PhD[1], Tiffany L. Dominguez, BS[1], Mehran Makvandi, PharmD[1], Hsiaoju Lee, PhD[1], Shihong Li, MS[1], Erin K. Schubert, BS[1], Daniel A. Pryma, MD[1], Michael D. Farwell, MD[1], Robert H. Mach, PhD[1], Fiona Simpkins, MD[2], Lilie L. Lin, MD[3], David A. Mankoff, MD, PhD[1], and Robert K. Doot, PhD[1]*

Author affiliations: [1]Department of Radiology, Perelman School of Medicine, University of Pennsylvania, Philadelphia, PA, USA. [2]Department of OBGYN, Division of Gynecology and Oncology, Perelman School of Medicine, University of Pennsylvania, PA, USA. [3]Department of Radiation Oncology, Division of Radiation Oncology, [3]The University of Texas MD Anderson Cancer Center, Houston, TX, USA

*Corresponding author:
Robert K. Doot, PhD
University of Pennsylvania
160A John Morgan Building
3620 Hamilton Walk
Philadelphia, PA 19104
Phone: (215) 573-6016
Fax: (215) 573-3880
Email: robdoot@pennmedicine.upenn.edu
https://orcid.org/0000-0003-1747-239X

First author:
Anthony J. Young
University of Pennsylvania
193 John Morgan Building
3620 Hamilton Walk
Philadelphia, PA 19104
Phone: (215) 746-0039
Fax: (215) 573-3880
Email: anthony.young@pennmedicine.upenn.edu

Word count:4990

Running title ^{18}F-FTT targets PARP-1 in ovarian cancer

ABSTRACT

The poly-(adenosine diphosphate-ribose) polymerase (PARP) family of proteins participates in numerous functions, most notably the DNA damage response. Cancer vulnerability to DNA damage has led to development of several PARP inhibitors (PARPi). This class of drugs has demonstrated therapeutic efficacy in ovarian, breast, and prostate cancers, but with variable response. Consequently, clinics need to select patients likely to benefit from these targeted therapies. *In vivo* imaging of ^{18}F-FluorThanatrace (^{18}F-FTT) uptake has been shown to correspond to PARP-1 expression in tissue. This study characterizes the pharmacokinetics of ^{18}F-FTT and tests kinetic and static models to guide metric selection in future studies assessing ^{18}F-FTT as a biomarker of response to PARPi therapy. Methods: Fourteen prospectively enrolled ovarian cancer patients were injected with ^{18}F-FTT and imaged dynamically for 60-minutes post-injection followed by up to two whole-body scans, with venous blood activity and metabolite measurements. Maximum and peak standardized uptake values (SUV_{max} and SUV_{peak}) were extracted from dynamic images and whole-body scans. Kinetic parameter estimates and SUVs were assessed for correlations with tissue PARP-1 immunofluorescence (n=7). Simulations of population kinetic parameters enabled estimation of measurement bias and precision in parameter estimates. Results: ^{18}F-FTT blood clearance was variable, but labeled metabolite profiles were similar across patients, supporting use of a population parent fraction curve. Total distribution volume (V_T) from a reversible two-tissue compartment model and Logan reference tissue distribution volume ratio (Logan DVR) from the first hour of PET acquisition correlated with tumor PARP-1 expression by immunofluorescence (r=0.76 and 0.83 respectively, p<0.05). DVR bias and precision estimates were 6.4% and 29.1%, respectively. SUV_{max} and SUV_{peak} acquired from images with midpoints of 57.5, 110±3, and 199±4 min highly correlated with PARP-1 expression (mean ± standard deviation, r≥0.79, p<0.05). Conclusion: Tumor SUV_{max} and SUV_{peak} at 55-60-minutes post-injection and later and DVR from ≥ 60-minutes appear to be robust non-invasive measures of PARP-1 binding. ^{18}F-FTT uptake in ovarian cancer was best described by models of reversible binding. However, pharmacokinetic patterns of tracer uptake were somewhat variable, especially at later time points.

KEY WORDS: PET, ^{18}F-FluorThanatrace, PARP inhibitor, ovarian cancer, radiotracer tissue pharmacokinetics.

INTRODUCTION

Poly-adenosine diphosphate-ribose polymerase inhibitors (PARPis) have demonstrated efficacy in a variety of cancers. Three PARPis (olaparib, rucaparib, and niraparib) are currently FDA approved for selected indications for ovarian cancers, and one, talazoparib, is approved for women with locally advanced or metastatic breast cancer with germline breast cancer gene mutations. The PARPi olaparib was initially approved in 2014 for advanced ovarian cancer patients with deleterious or suspected deleterious germline breast cancer gene mutations following treatment with three or more lines of chemotherapy. Since then, additional indications have included patients with response to platinum-based chemotherapy, another marker for DNA repair defects (*1*). However, PARPi efficacy for approved ovarian cancer indications is variable, providing the impetus to develop non-invasive biomarkers to measure the entire burden of disease and better guide selection of targeted therapies containing PARPis (*2*). With this goal, the positron emission tomography (PET) radiotracer ^{18}F-FluorThanatrace (^{18}F-FTT) has been developed as a non-invasive *in vivo* measure of PARP-1 expression (*3,4*).

^{18}F-FTT has been evaluated in preclinical models (*3*) and cancer patients (*4*). The Makvandi et al. human ovarian cancer study demonstrated correlation between static PET uptake measures and PARP-1 expression in tissue measured by immunohistochemistry and autoradiography (*5*). A wide range of ^{18}F-FTT uptake was seen in ovarian cancer patients, ranging from background maximum voxel standard uptake value (SUV_{max}) of 2 to above 12-g/mL (*5*). Similar studies are underway in other cancers, including breast (*6*), pancreatic, prostate, and glioblastoma (*2*).

In this companion study, we analyzed pharmacokinetics of ^{18}F-FTT PET uptake in 14 ovarian cancer patients by expanding PET data from one static PET scan reported in Makvandi et al. (*5*) to include a one-hour dynamic acquisition and optional second static scan for up to 3 same day PET scans per subject. Our results include 7 previously reported SUVs from the parent study (*5*). Kinetic parameters derived from graphical and compartmental models were compared to tissue

PARPi expression assays to inform selection of imaging metrics and timing for PET image acquisition. Computer simulations were used to study model behavior under typical conditions. Static SUVs and SUV-to-normal tissue ratios were compared to kinetic parameters to guide selection of clinic-friendly imaging protocols.

MATERIALS AND METHODS

Clinical Trial

Women with known or suspected recurrent or metastatic epithelial ovarian cancer were enrolled and gave informed consent for University of Pennsylvania Institutional Review Board approved prospective clinical trial of ^{18}F-FTT PET/CT imaging (NCT02637934) between January 2016 and January 2017 at the Hospital of the University of Pennsylvania. The study protocol is described at clinicaltrials.gov. Surgical or biopsy samples were analyzed for PARP-1 expression using immunofluorescence assays. For a detailed description of this clinical trial and tissue analysis methods, see Makvandi et al. including supplemental materials (5). Patients were separated into dynamic and dosimetry imaging cohorts.

Imaging Protocol

Synthesis of ^{18}F-FTT was described previously (3). PET/CT imaging was performed on an Ingenuity TF scanner (Philips Healthcare, Andover, MA) (7) over one field-of-view for 60-minutes following radiotracer injection of ^{18}F-FTT (389±37 MBq). Up to 2 whole-body scans were acquired, beginning 90 and 180-minutes post-injection. Dynamic PET acquisitions were reconstructed (7) into 50 frames consisting of 24x5-s, 6x10-s, 3x20-s, 2x30-s, 5x60-s, and 10x300-s durations.

Venous Blood Sampling and Analysis

Venous blood was sampled at approximately 2, 5, 10, 30, 60, and 240-min post-injection to measure radiometabolites. Activity concentrations in whole blood and plasma were counted using

a WIZARD[2] 2480 gamma counter (Perkin Elmer, Waltham, MA). Acetonitrile-treated plasma supernatant was analyzed in Agilent 1260 Infinity Series (Agilent Technologies, Santa Clara, CA, USA) high performance liquid chromatology system using Agilent ZORBAX StableBond C18 column via mobile phase of 51% methanol and 49% 0.1M ammonium formate buffer with sample radiochromatogram in Suppl. Fig. 1.

Image Analysis

PET image processing was performed using MIM v6.9 (MIM Software Inc., Cleveland, OH), with spherical volumes of interest (VOIs) drawn around tumor and background regions; a board-certified nuclear medicine physician (ARP) verified placement. Time-activity-curves for tumor SUV_{max} and SUV_{peak} with and without partial volume correction were used for kinetic analysis. SUV_{peak} was automatically positioned as the 1-cm^3 volume with greatest mean activity for each image frame (*8*). Partial volume correction (PVC) of SUV measures was performed as previously described (*9*), utilizing a normal muscle background region. Image blood pool SUV_{peak} was measured in iliac artery for 10 patients with abdominal imaging, or descending aorta for 4 patients with thoracic imaging. Background muscle activity was estimated using a 20-mm-diameter VOI in gluteus or paraspinal musculature. Tumor-to-normal muscle activity ratios were calculated by dividing tumor activity by average background. Whole-body scan data was added to dynamic data after correcting for timing of the 2-3 bed positions covering a VOI.

Kinetic Analysis

Kinetic analysis of radiotracer uptake was performed using PMOD v3.7 (PMOD Technologies Ltd., Zurich, Switzerland). Individual parent fraction data was corrected for plasma protein binding, averaged between patients, and fitted sigmoidally, creating a population ^{18}F-FTT parent fraction function to correct blood inputs for labeled metabolites. Tumor blood volume fractions were assumed to vary within 0.01-0.40, with upper bound based on literature values for malignant ovarian cancer (*10*) and lower bound at a minimal physiologically relevant value.

Image-extracted blood input curves were fitted to tri-exponential functions and corrected for population average plasma partitioning. Initial parameters and bounds were selected to encompass expected parameter ranges, Suppl. Table 1. Compartmental models were initially fit using data from the dynamic and both static scans. For comparison, models were fit with dynamic plus first whole-body scan, 0-60min dynamic, and truncated 0-30-minute datasets. Reported results are from 0-60-min dynamic dataset unless stated otherwise.

Tumor kinetics were analyzed using reversible models of ^{18}F-FTT binding: aforementioned 2CR model and reversible graphical method. Logan's reference tissue (*11*) graphical technique was used to estimate tumor distribution volume ratio (DVR) without needing blood activity or metabolite measurements, and to compensate for possible low level non-specific uptake. Since population t* was 40-min, this model was not evaluated on 0-30-min data. Positive efflux rate terms k_2' of transfer from muscle to plasma were averaged and used for all patients via multilinear reference tissue model (*12*).

Statistics

Comparisons between kinetic model complexity and effectiveness were evaluated via PMOD calculated Akaike information criterion (AIC) (*13*).

Static tumor SUV, tumor-to-normal muscle ratios, 2CR V_T, and Logan reference model DVR estimations were each tested for correlation with 7 PARP-1 tumor immunofluorescence (IF) values with IF methods reported in Makvandi et. al. supplemental materials (*5*).

Two-tailed Pearson's r was calculated in SPSS25 (IBM Armonk, NY, USA) and used to assess correlations between tissue IF and imaging data; correlations with a p-value ≤ 0.05 were considered significant against the null hypothesis r=0.

Kinetic Model Performance

Sensitivity curves were calculated as percent change in model output corresponding to 1% change in each parameter. Repeatability of kinetic parameter estimation was analyzed using simulated data based on ranges of individual kinetic parameters via methods of Viswanath et al. (*14*). Bias was averaged across each of 100 noise realizations, and averaged across 200 runs. Precision for each run was calculated as average standard deviation across all noise realizations, divided by true value.

RESULTS

Twenty women with recurrent or metastatic epithelial ovarian cancer, age ranging from 21 to 70-years, gave informed consent and were enrolled in the University of Pennsylvania Institutional Review Board approved clinical trial NCT02637934 between January 2016 and January 2017. A trial diagram overview was published previously (*5*). Eighteen patients were imaged with ^{18}F-FTT PET/CT, and sixteen completed venous blood sampling with no reported adverse events.

Of the 18 patients, a dynamic imaging cohort of 14 was scanned for 60-minutes post-injection, followed by 90 and 180-min post-injection skull base to mid-thigh (whole-body) static scans. Blood data from 4 subjects in dosimetry cohort were included in population blood results. Tumors were visible in dynamic fields-of-view for 10 patients, 7 of whom had surgical tumor tissue samples and accompanying PARP-1 immunofluorescence (IF) assays. Static scans measured tumor activity at 110±3 (mean±standard deviation) and 199±4-min post-injection. Representative PET and fused PET/CT images are in Fig. 1.

Tumor ^{18}F-FTT uptake, as measured by SUV_{max} and SUV_{peak}, generally increased over 60-min dynamic scan and subsequent static scans, with more variable behavior after 60-min (Fig. 2). SUV_{max} at 55-60-minutes post-injection was 4.2±2.0 g/mL, and SUV_{peak} was 3.4±1.6 g/mL. Normal muscle, bone, and blood pool activities (representative patient in Fig. 3) were fairly stable over

time, and used for kinetic modeling and SUV ratios. Tumor-to-normal muscle SUV ratios were 2.6±1.1 for SUV_{max} and 2.1±0.9 for SUV_{peak}. Partial volume corrections based on tumor size and normal muscle background resulted in SUV increases, Suppl. Table 2.

Blood sampling and processing was performed on sixteen patients. Results from samples at 240-minutes post-injection were omitted due to high error from low counts. ^{18}F-FTT blood inputs demonstrated some variability between patients. Differences were also noted based on location of blood pool VOI, related to partial volume effects and dispersion of tracer from the larger aorta to the iliac arteries Fig. 4, Suppl. Fig. 2. Plasma to whole blood partitioning was stable throughout imaging at a ratio of 1.26±0.02, Suppl. Fig. 3, and between patients, 1.26±0.08, n=16, and input into kinetic models as a constant parameter. ^{18}F-FTT was metabolized, reaching an average parent percentage of 59±10% at 60-minutes as seen in Fig. 5. The resulting population parent fraction curve was used to correct image-derived, individual blood input function for metabolites prior to kinetic analyses. Metabolites were not included in the model tissue compartments, assuming there was no specific uptake of polar metabolites.

Model fit AICs (*13*) were 273±24 for the two-tissue compartment model with reversible binding (2CR) , 292±18 for two-tissue compartment with irreversible binding ($k_4=0$), and 340±34 for one-tissue compartment model. Example fits for model curves in a representative tumor are provided in Fig. 6. In 33 of 39 cases 2CR outperformed the irreversible model and had lower AICs than the one-tissue compartment model in every case. 2CR was therefore used for all subsequent compartmental analysis.

Sensitivity curves of 2CR parameters are provided in Suppl. Fig. 4. Blood volume fraction (vB) and K_1 exhibited early influence, followed by K_1/k_2, k_3, and k_4.

When model parameters V_T and DVR of fitted tumor SUV_{max} and SUV_{peak} time-activity-curves with and without partial volume correction were compared with reference standard PARP-1 IF, SUV_{peak} based kinetics correlations were slightly higher, therefore reported kinetic analyses and

simulations used SUV_{peak}.

The Logan reference tissue model with normal muscle was tested as a graphical model of reversible tracer binding that does not require blood sampling. The population k_2' value used in Logan reference tissue modeling was $0.022\pm0.022\text{-}min^{-1}$ using positive k_2' values from 7 patients. Logan normal muscle DVR was 2.2 ± 1.2, n=9 excluding one patient with excessive motion.

Associations between PARP-1 IF and tumor uptake, with both static uptake measures and kinetic parameters, were examined. Associations between static measures of tumor uptake and PARP-1 IF varied with image timing. SUV_{max} and SUV_{peak} obtained after 55-min (57.5, ~110, and ~119-min) demonstrated statistically significant correlations, Table 1. Partial volume corrections did not substantially change correlations. Tumor-to-normal muscle uptake ratios showed similar or slightly worse associations with PARP-1 expression as compared to uncorrected SUVs, Table 1. V_T significantly correlated with tissue PARP-1 IF for only the one-hour dynamic data set, r=0.76, p<0.05, (Table 2, Fig. 7A). DVR using normal muscle was significantly correlated with tissue IF (r=0.83, p<0.05, n=7), but not with SUVs at 55-60-minutes (r=0.41, p>0.05, n=10), until after dynamic acquisition input data was expanded to include measures from one or two subsequent whole-body scans (r≥0.81, p<0.05, n=10) (Table 3, Fig. 7B).

Bias and precision estimates from simulations in Table 4 found Logan DVR had lowest bias of 6% and best precision of 29%.

DISCUSSION

We studied several PET measures of ^{18}F-FTT uptake in ovarian cancer to inform recommendations of metrics and imaging protocols for measuring PARP-1 expression. SUVs and kinetic parameters from dynamic imaging analysis correlated with PARP-1 IF pathology measures. However, additional ^{18}F-FTT imaging studies of patients participating in PARPi

treatment trials will be required to determine if ^{18}F-FTT imaging can serve as a biomarker for response to PARPi therapy.

The superior fit for 2CR to patients' tumors (Fig. 6), superior AIC values versus other compartmental models, and high association of reversible model tumor DVR with PARP-1 IF support characterization of ^{18}F-FTT as having substantial reversible binding *in vivo* during the imaging session. Makvandi et al. reported a correlation r^2=0.60 (n=10 lesions) between PARP-1 IF and SUV_{max} (*5*). Our corresponding r^2=0.64 (or equivalently r=0.80 in Table 1) is slightly different due to our smaller n=7 only including cancerous lesions within fields-of-view for the dynamic scans. More clinic-friendly SUV_{max} and SUV_{peak} measures' high correlation with PARP-1 expression supports their use as potentially robust and repeatable metrics for measurement of *in vivo* PARP-1, with the benefit that SUVs do not require assumptions of reversible or irreversible binding.

Although best described by a reversible model, late uptake of ^{18}F-FTT also suggest a degree of irreversible binding, possibly indicative of PARP trapping, as many patients' time-activity-curves showed increases in uptake in static scans at 110 and 199-minutes, Fig. 2. The impact of this variability on the accuracy of kinetic estimates of tracer binding may be complicated by model and input function source selections, as the compartmental model was more sensitive to k_3 and k_4 parameters at later times, Suppl. Fig. 4, when variable uptake of metabolites and/or issues with the image derived input functions could interfere with parameter estimates. Without prior dynamic data in humans or preclinical-based models to provide physiologic bounds on model fitting, these parameters were highly variable within this patient population. Simulations, Table 4, and Suppl. Fig. 5 show potential for large errors in fitted 2CR V_T. This dataset is not sufficient to rule out an element of irreversible binding of ^{18}F-FTT to PARP-1 within the time frame of 200-min post-injection.

Although both DVR measures from 0-60-minutes and 55-60-minute SUVs correlated with

PARP-1 IF tissue assay results, these measures did not correlate with each other. Adding late uptake time points from whole-body scans measures to the dynamic dataset, however, resulted in significant correlation between DVR and SUVs (r>0.81, p<0.01). Conversely, adding additional static scans to dynamic dataset for 2CR model resulted in decreased correlations between V_T and both PARP-1 IF and SUVs, Table 3. DVR's better correlations to SUV when using longer duration data sets could be due to the DVR graphical reference technique not requiring metabolite corrections. It is also possible that DVRs are better able to account for some non-selective, irreversible parent or metabolite binding at later time points via use of a reference region. Another possibility is the existence of an inflection point in the binding characteristics that is not captured with the gap in imaging between 60 and about 110-minutes, which may impact V_T estimations.

Metabolism, plasma to whole blood partitioning, and plasma protein binding of ^{18}F-FTT were similar within this population, supporting use of averaged population values and functions for kinetic analyses, Fig. 5 and Suppl. Fig. 3. Our reported ^{18}F-FTT plasma to whole blood partitioning ratio of 1.26 in Suppl. Fig. 3 was similar to a ratio of 1.28 (reported as a 0.781 blood to plasma ratio) for another rucaparib analog radiotracer, ^{14}C-rucaparib, in a cohort of six patients with confirmed advanced solid tumor (*15*). This ^{14}C-rucaparib study (*15*) also used mass spectrometry to determine that 64%±13.7% of the labeled components was the parent radiotracer in pooled plasma samples from 1-hour to 24-hours post-injection, which was similar to our reported average parent ^{18}F-FTT percentage of 59±10% at one hour. We have not identified these metabolites or their binding properties, except that they are more polar than ^{18}F-FTT, similarly to rucaparib metabolites, which are carboxylated at the n-methyl substituent.

Individual image derived blood input curves were influenced by VOI positioning, suggesting partial volume effects may influence our blood pool measurements in lower torso. This is most apparent in later time points where blood pool approaches the activity level of surrounding tissue and remains above sampled blood activity, Figs. 3 and 4. Lower adjacent background activity

(spillover) for VOIs in descending aorta as compared to VOIs in iliac arteries potentially biased measured activity based on differences in the arterial internal diameters. Reduced artery size contributes to increased partial volume effects, and the 1-cm^3, or 12.4-mm diameter, peak VOIs used for calculating blood activity are above the luminal diameter of the common iliac artery, reported to be 8.8±1.2-mm in women (*16*), and thus more impacted than the larger descending aorta at 13.7±1.9 to 16.6±3.0-mm. The full width half max resolution of the Ingenuity PET scanner of 4.8-mm (*7*) also limits the ability to use significantly smaller VOIs within small vessels. Using venous blood sampling instead of arterial sampling also limits our ability to verify the arterial blood input function extracted from image blood pools.

Variable levels of background uptake in surrounding tissue support use of background corrections to quantitate ^{18}F-FTT uptake. In this study of ovarian cancer, however, there was little impact of partial volume corrections on correlations with tissue PARP-1 expression, in contrast to work in breast cancer imaging of ^{18}F-FTT uptake (*6*), potentially due to very low levels of background uptake in breast tissue in comparison with higher background uptake in muscle surrounding most ovarian lesions. Partial volume correction of tumor-to-normal muscle ratios similarly did not have a substantial effect on correlations with PARP-1 IF, Table 1.

As noted, we found somewhat variable tumor kinetics late after tracer injection, potentially the result of variable trapping of the PARP inhibitor analog, ^{18}F-FTT, or tissue uptake of metabolites, which account for 30% to 50% of circulating blood radioactivity at 60-minutes. This concern and the good correlation between 57.5-min ^{18}F-FTT SUV$_{max}$ and SUV$_{peak}$ measures with PARP-1 IF tissue assay results support a recommendation for imaging 60-minutes post-injection for static uptake measures. To better inform image quantification and kinetic analysis methods, additional studies with longer dynamic acquisitions of at least 90-min with arterial blood sampling and a higher percentage of tumors receiving ex vivo assays of PARP-1 expression would be helpful. However, it may prove difficult to recruit sufficient cancer patients who could tolerate longer

imaging times and accept more invasive arterial blood sampling. Preclinical experiments to assess the degree to which ^{18}F-FTT binding within cells is reversible during the first 2 hours of ^{18}F-FTT uptake would inform future selection of kinetic analysis techniques and possibly ideal post-injection time range for static SUV measures of tumor uptake.

CONCLUSION

Pharmacokinetics of ovarian cancer uptake of ^{18}F-FTT suggest SUVs from whole-body PET scans acquired 60-minutes post-injection are a robust metric for non-invasively quantifying PARP-1 expression *in vivo*. Although the Logan normal muscle reference tissue model is a promising kinetic analysis technique for quantitating ^{18}F-FTT uptake, there is not yet sufficient evidence that kinetic estimates or tumor-to-normal muscle SUV ratios represent substantial improvements over more clinic-friendly SUV_{max} or SUV_{peak} tumor measures to justify dynamic scanning for larger-scale trials of ^{18}F-FTT PET. More preclinical and human ^{18}F-FTT studies would be valuable to elucidate underlying reversible and irreversible ^{18}F-FTT binding mechanisms and guide future ^{18}F-FTT studies, especially in the study of PARP inhibitor dosing and pharmacodynamics and utility as a biomarker.

DISCLOSURE

KEY POINTS

QUESTION: Can characterization of pharmacokinetics of ovarian cancer uptake of ^{18}F-FTT inform selection of uptake quantitation methods and post-injection timing of PET acquisition?

PERTINENT FINDINGS: Prospective clinical trial of human ovarian cancer patients found SUV and DVR quantitation of ^{18}F-FluorThanatrace tumor uptake significantly correlated with PARP-1 expression.

IMPLICATIONS FOR PATIENT CARE: ^{18}F-FluorThanatrace scans may one day select patients likely to benefit from PARP inhibitor therapy and serve as a tool to monitor response.

REFERENCES

1. Franzese E, Centonze S, Diana A, et al. PARP inhibitors in ovarian cancer. *Cancer Treat Rev*. 2019;73:1-9.

2. Ambur Sankaranarayanan R, Kossatz S, Weber W, Beheshti M, Morgenroth A, Mottaghy FM. Advancements in PARP1 targeted nuclear imaging and theranostic probes. *J Clin Med*. 2020;9:2130.

3. Zhou D, Chu W, Xu J, et al. Synthesis, [^{18}F] radiolabeling, and evaluation of poly (ADP-ribose) polymerase-1 (PARP-1) inhibitors for in vivo imaging of PARP-1 using positron emission tomography. *Bioorg Med Chem*. 2014;22:1700-1707.

4. Michel LS, Dyroff S, Brooks FJ, et al. PET of Poly (ADP-Ribose) Polymerase activity in cancer: Preclinical assessment and first in-human studies. *Radiology*. 2017;282:453-463.

5. Makvandi M, Pantel A, Schwartz L, et al. A PET imaging agent for evaluating PARP-1 expression in ovarian cancer. *J Clin Invest*. 2018;128:2116-2126.

6. McDonald ES, Doot RK, Pantel AR, et al. Positron emission tomography imaging of poly–(adenosine diphosphate–ribose) polymerase 1 expression in breast cancer: A nonrandomized clinical trial. *JAMA Oncol*. 2020;6:921-923.

7. Kolthammer JA, Su K-H, Grover A, Narayanan M, Jordan DW, Muzic RF. Performance evaluation of the Ingenuity TF PET/CT scanner with a focus on high count-rate conditions. *Phys Med Biol*. 2014;59:3843-3859.

8. Wahl RL, Jacene H, Kasamon Y, Lodge MA. From RECIST to PERCIST: Evolving considerations for PET response criteria in solid tumors. *J Nucl Med*. 2009;50 Suppl 1:122S-50S.

9. Peterson LM, Mankoff DA, Lawton T, et al. Quantitative imaging of estrogen receptor expression in breast cancer with PET and ^{18}F-fluoroestradiol. *J Nucl Med*. 2008;49:367-374.

10. Thomassin-Naggara I, Balvay D, Aubert E, et al. Quantitative dynamic contrast-enhanced MR imaging analysis of complex adnexal masses: a preliminary study. *Eur Radiol*. 2012;22:738-45.

11. Logan J, Fowler JS, Volkow ND, Wang GJ, Ding YS, Alexoff DL. Distribution volume ratios without blood sampling from graphical analysis of PET data. *J Cereb Blood Flow Metab*. 1996;16:834-840.

12. Ichise M, Liow JS, Lu JQ, et al. Linearized reference tissue parametric imaging methods: application to [^{11}C]DASB positron emission tomography studies of the serotonin transporter in human brain. *J Cereb Blood Flow Metab*. 2003;23:1096-112.

13. Akaike H. A new look at the statistical model identification. *IEEE Trans Autom Control*. 1974;19:716-723.

14. Viswanath V, Zhou R, Lee H, et al. Kinetic modeling of 18F-(2S,4R)4-fluoroglutamine in mouse models of breast cancer to estimate glutamine pool size as an indicator of tumor glutamine metabolism. *J Nucl Med*. Epub ahead of print December 4, 2020.

15. Liao M, Watkins S, Nash E, et al. Evaluation of absorption, distribution, metabolism, and excretion of [^{14}C]-rucaparib, a poly(ADP-ribose) polymerase inhibitor, in patients with advanced solid tumors. *Invest New Drugs*. 2020;38:765-775.

16. Pedersen OM, Aslaksen A, Vik-Mo H. Ultrasound measurement of the luminal diameter of the abdominal aorta and iliac arteries in patients without vascular disease. *J Vasc Surg*. 1993;17:596-601.

FIGURES
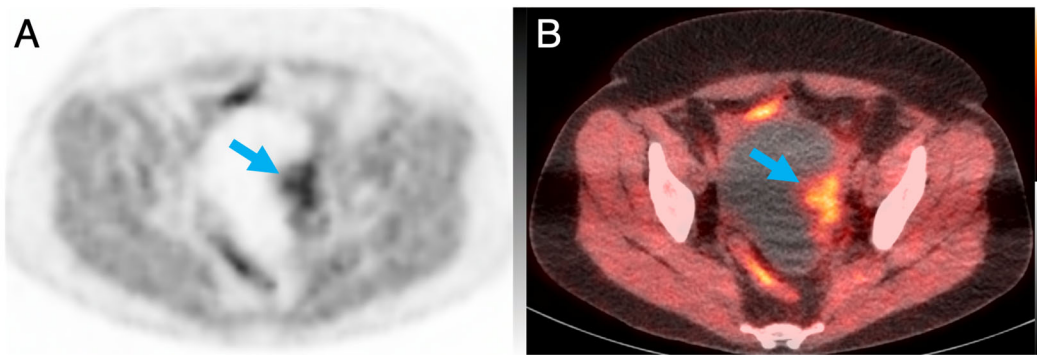
Figure 1: Patient 4's PET (A) and fused PET/CT (B) images 108-minutes post-injection with blue arrow indicating tumor with SUV_{max} of 5.6 g/mL. Scaled 0-5 g/mL SUV and -160 to +240 HU CT.
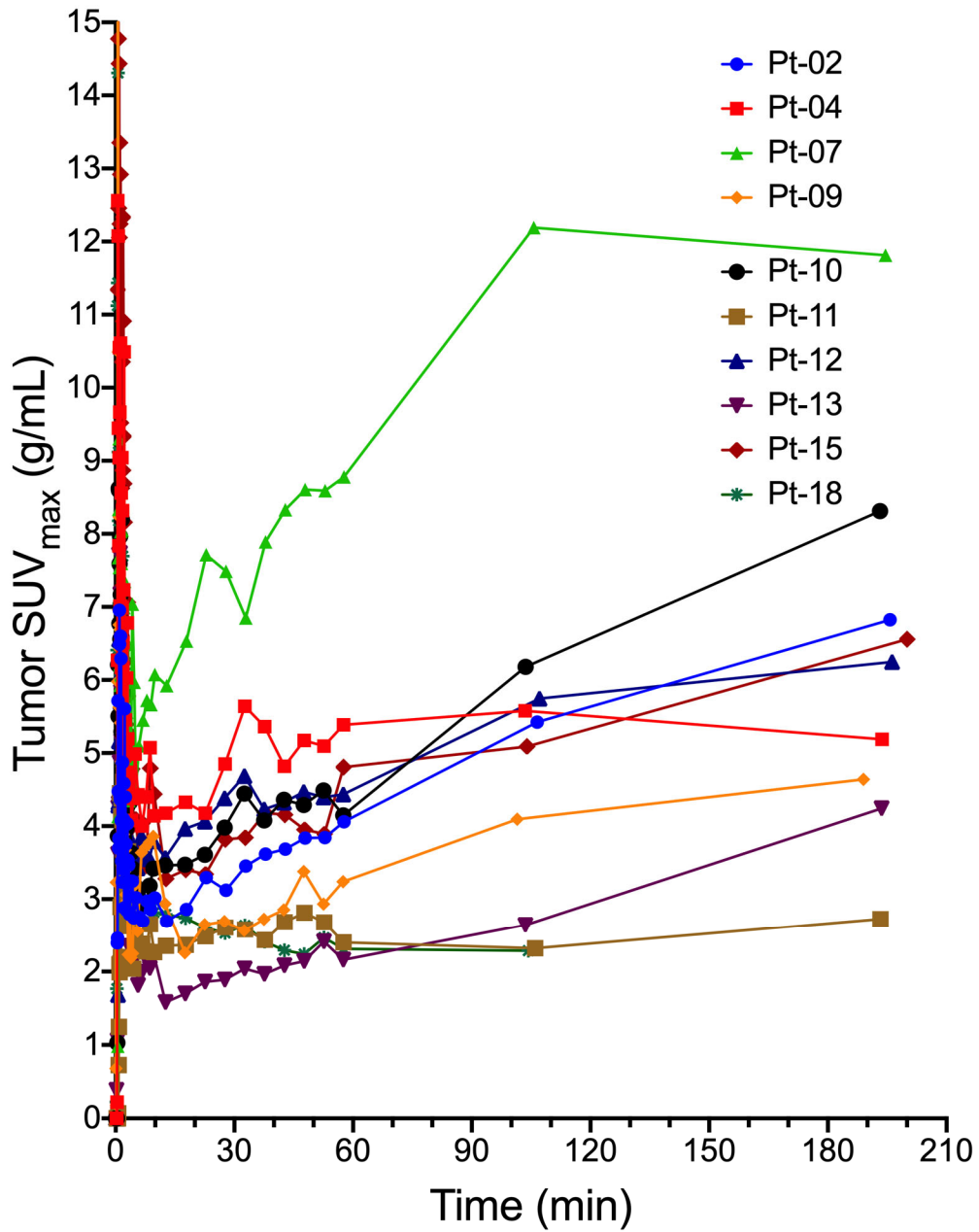
Figure 2: ^{18}F-FTT index lesion max uptake over time for 10 subjects. The first 60-minutes of scanning is from the dynamic acquisition, followed by static scan tumor measurements at 110±3 and 199±4 minutes from 2 subsequent whole-body PET scans.
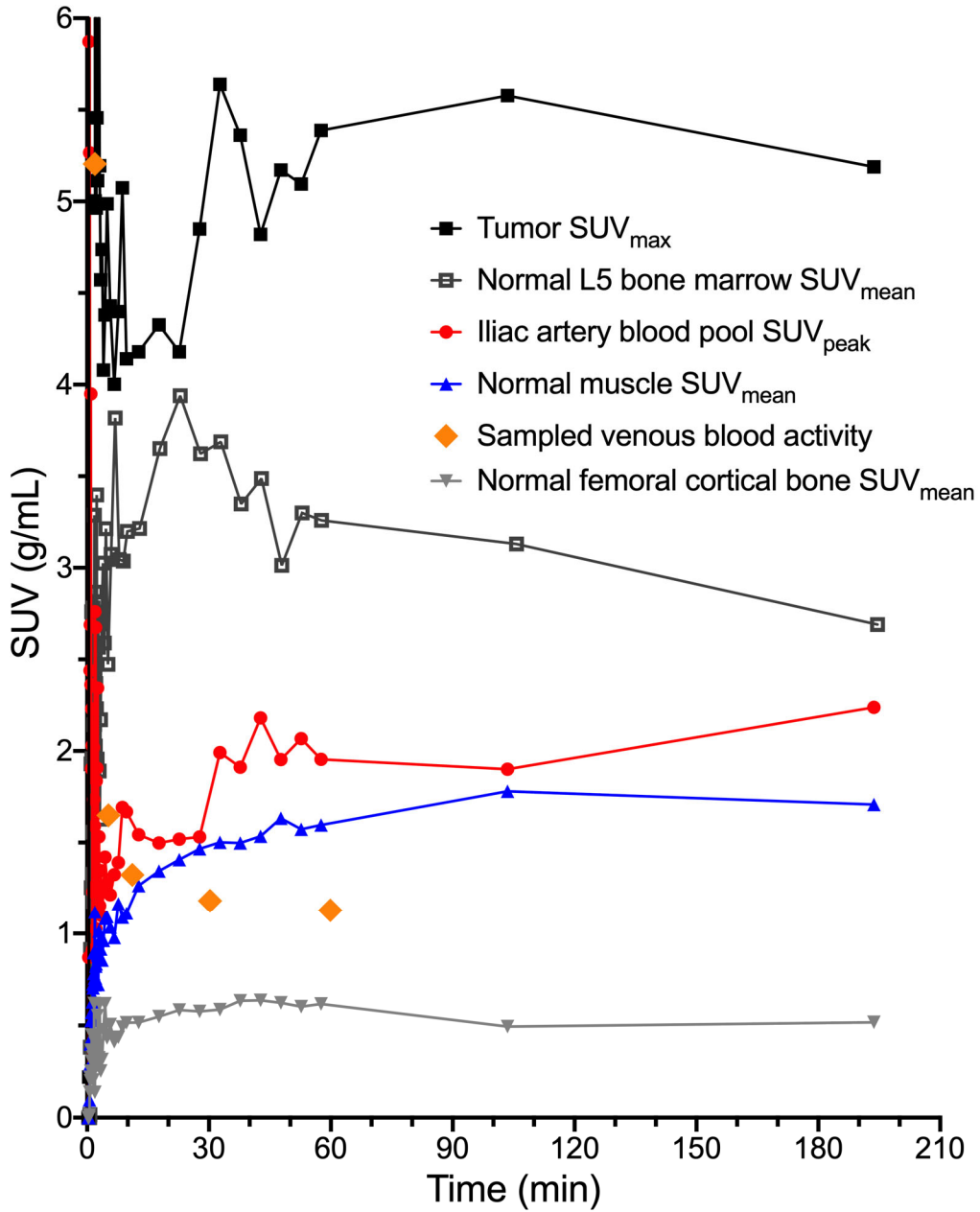
Figure 3: Patient 4 time-activity-curves for one-hour dynamic acquisition following injection and 2 subsequent whole-body PET/CT scans.
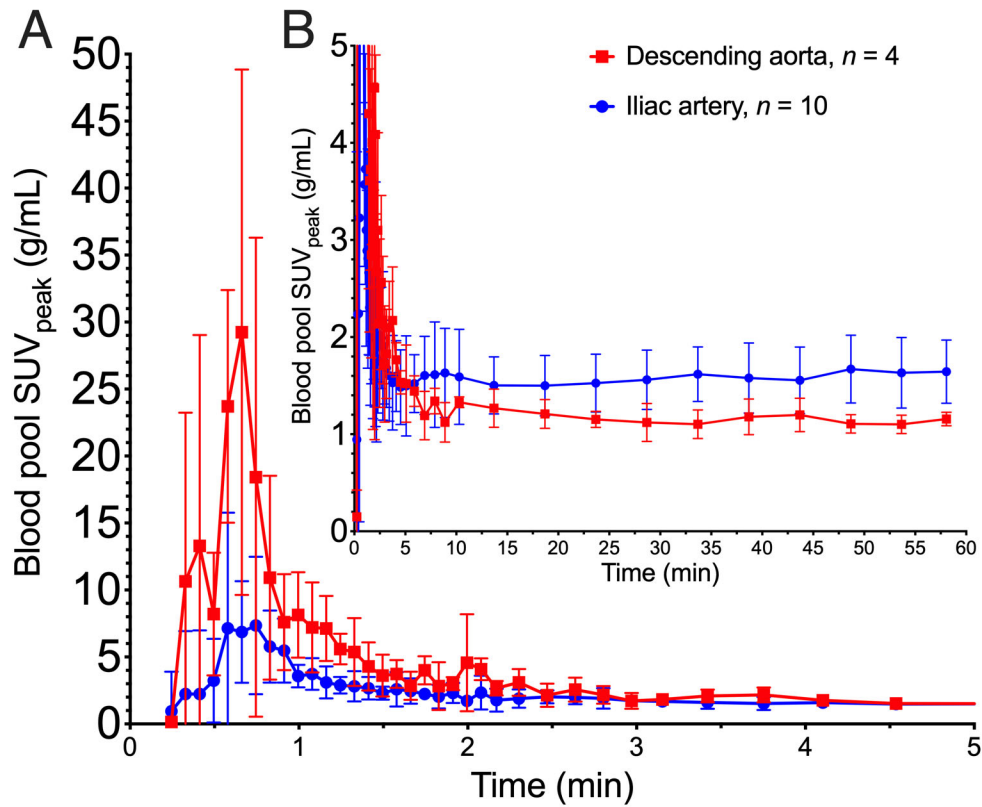
Figure 4: Population average blood input functions for descending aorta (n=4) and iliac artery (n=10). Values are mean ± standard deviation. A is from 0-5-minutes post-injection scaled to highlight initial bolus. B is 0-60-minutes scaled to show late activity.
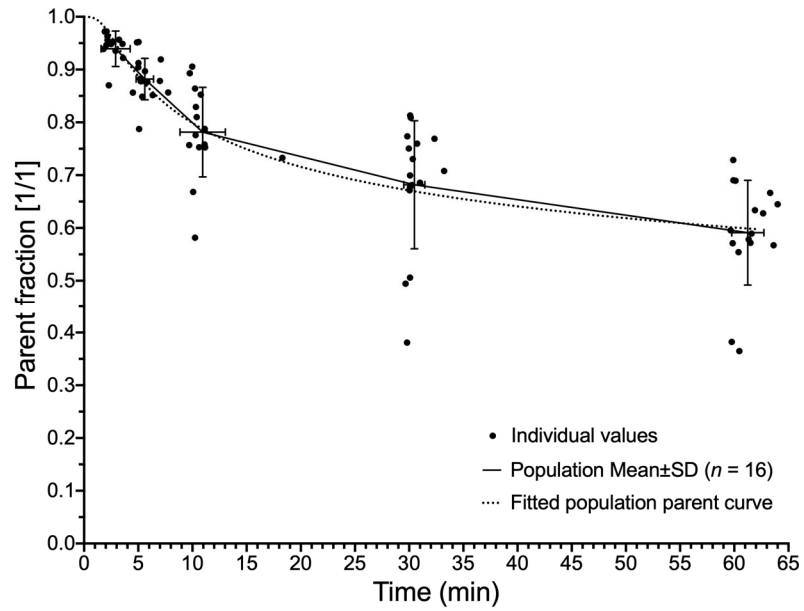
Figure 5: ^{18}F-FTT population parent fraction curve. Fitting was performed on population mean values, using a sigmoidal function. Fitted equation was used for parent fraction corrections for all kinetic modeling blood input curves and was of form $((1-t^3/(t^3+10^A))^B+C)/(1+C)$, where A=6.504, B=0.053, and C=1×10^{-8}, with time post-injection, t (in seconds).
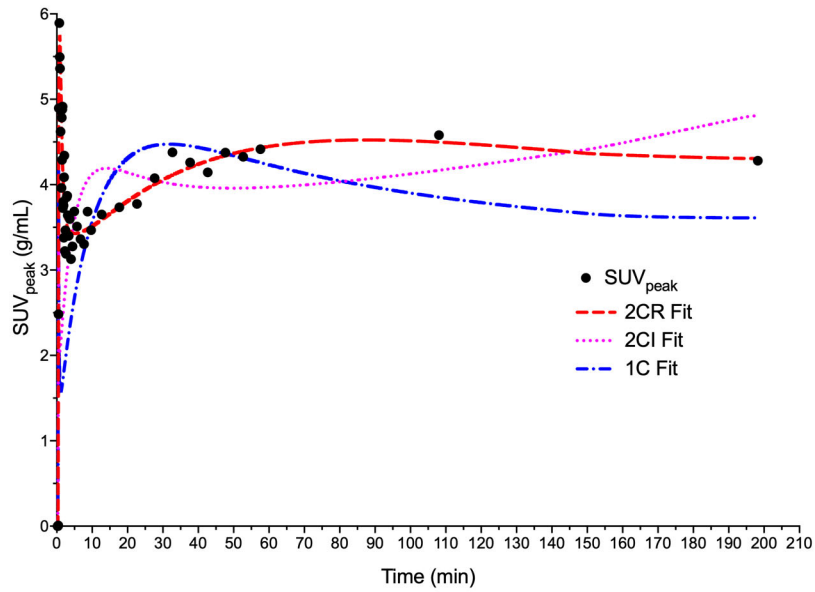
Figure 6: Patient 4 modeled time-activity-curves with one-tissue compartment reversible (1CR), two-tissue compartment reversible (2CR), and two-tissue compartment irreversible (2CI) model fits. Model Akaike information criterions (AIC) were 432, 336, and 401 for the 1CR, 2CR, and 2CI models, respectively.
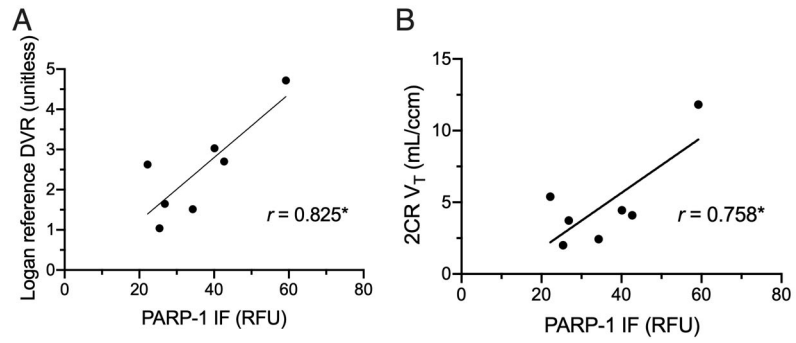
Figure 7: Correlation plots between kinetic parameters and PARP-1 immunofluoresence (n=7) in relative fluorescence units (RFU). Logan reference tissue DVR in A, two-tissue compartment (2CR) V_T in B *p<0.05.

TABLES

TABLE 1: Correlations between ^{18}F-FTT SUVs (g/mL) and unitless SUV ratios at different mid-bin times against PARP-1 IF (n=7).

PARP-1 IF versus	32.5min*, r	57.5min*, r	110±3min, r	199±4min, r
SUV$_{max}$	0.656	0.796†	0.800†	0.819†
SUV$_{peak}$	0.686	0.787†	0.855†	0.825†
PVC SUV$_{max}$	0.657	0.795†	0.799†	0.818†
PVC SUV$_{peak}$	0.684	0.786†	0.854†	0.823†
SUV$_{max}$ /NM‡	0.445	0.696	0.741	0.706
SUV$_{peak}$ /NM‡	0.512	0.707	0.808†	0.734
PVC SUV$_{max}$ /NM‡	0.454	0.700	0.318	0.531
PVC SUV$_{peak}$ /NM‡	0.515	0.710	0.808†	0.737

*Duration of dynamic frame was 5-minutes

†p<0.05

‡Normal muscle

TABLE 2: Kinetic measures from different total duration input data correlations with PARP-1 immunofluorescence.

PARP-1 IF versus	0-30min, r	0-60min, r	0-60+110min, r	0-60+110+199min, r
2CR* V_T (mL/cm^3)	0.415	0.758†	0.407	0.555
Logan NM‡ DVR§	-	0.825†	0.869†	0.822†

*Two-tissue compartment model with reversible binding ($k_4>0$)

†p<0.05

‡Normal muscle reference tissue

§Graphical methods not performed for 0-30-minute dataset

TABLE 3: Kinetic measure correlations with SUV_{peak} (n=10).

	57.5min SUV_{peak}, r	110±3min SUV_{peak}, r	199±4min SUV_{peak}, r
2CR* V_T (0-60min)	0.929[†]	0.974[†]	0.940[†]
2CR* V_T (0-60+110min)	0.082	0.259	0.365
2CR* V_T (0-60+110+199min)	0.548	0.722[†]	0.781[†]
Logan NM DVR[‡] (0-60min)	0.410	0.265	0.083
Logan NM DVR (0-60+110min)	0.879[†]	0.976[†]	0.969[†]
Logan NM DVR (0-60+110+199min)	0.806[†]	0.915[†]	0.974[†]

*Two-tissue compartment model with reversible binding ($k_4 > 0$)
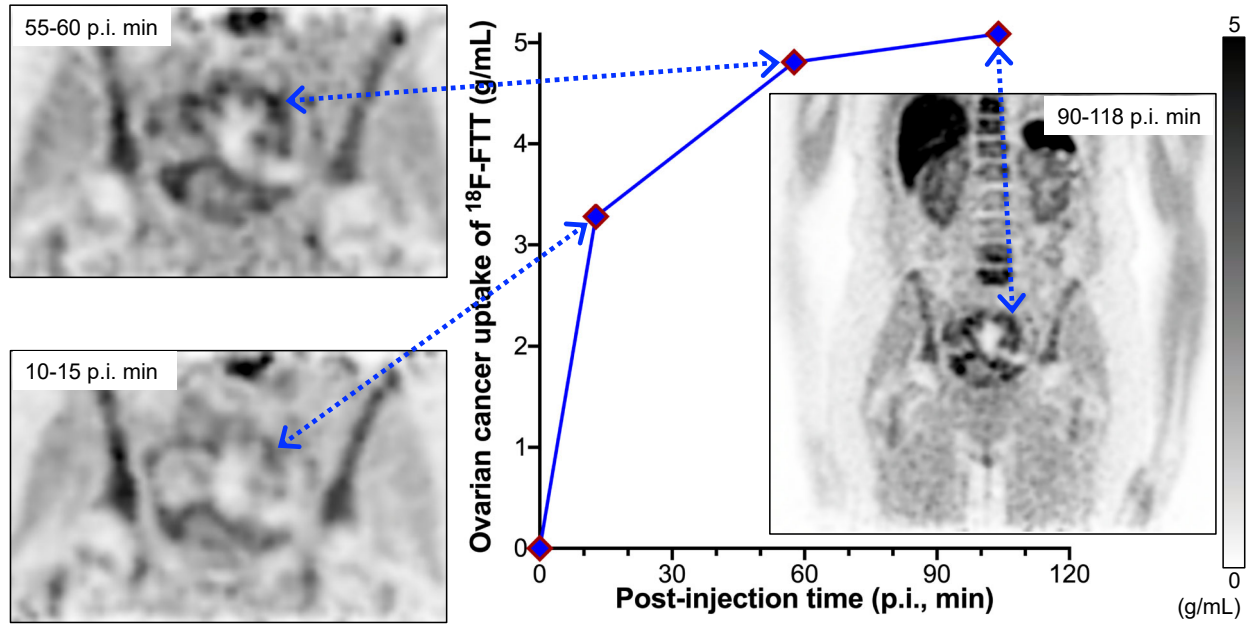
[†]$p < 0.05$

[‡]Normal muscle reference tissue

TABLE 4: Estimates of kinetic model parameter bias and precision.

|	Bias	Precision
2CR* V_T (mL/cm^3)	250%	635%
2CR K_1 (mL/cm^3/min)	-8%	54%
Logan DVR[†] (unitless)	6%	29%

*Two-tissue compartment model (2CR)

[†]Distribution volume ratio (DVR)

Graphical Abstract

SUPPLEMENTAL MATERIALS for Kinetic and static analysis of poly (adenosine diphosphate - ribose) polymerase-1 (PARP-1) targeted ^{18}F-FluorThanatrace (^{18}F-FTT) PET images of ovarian cancer
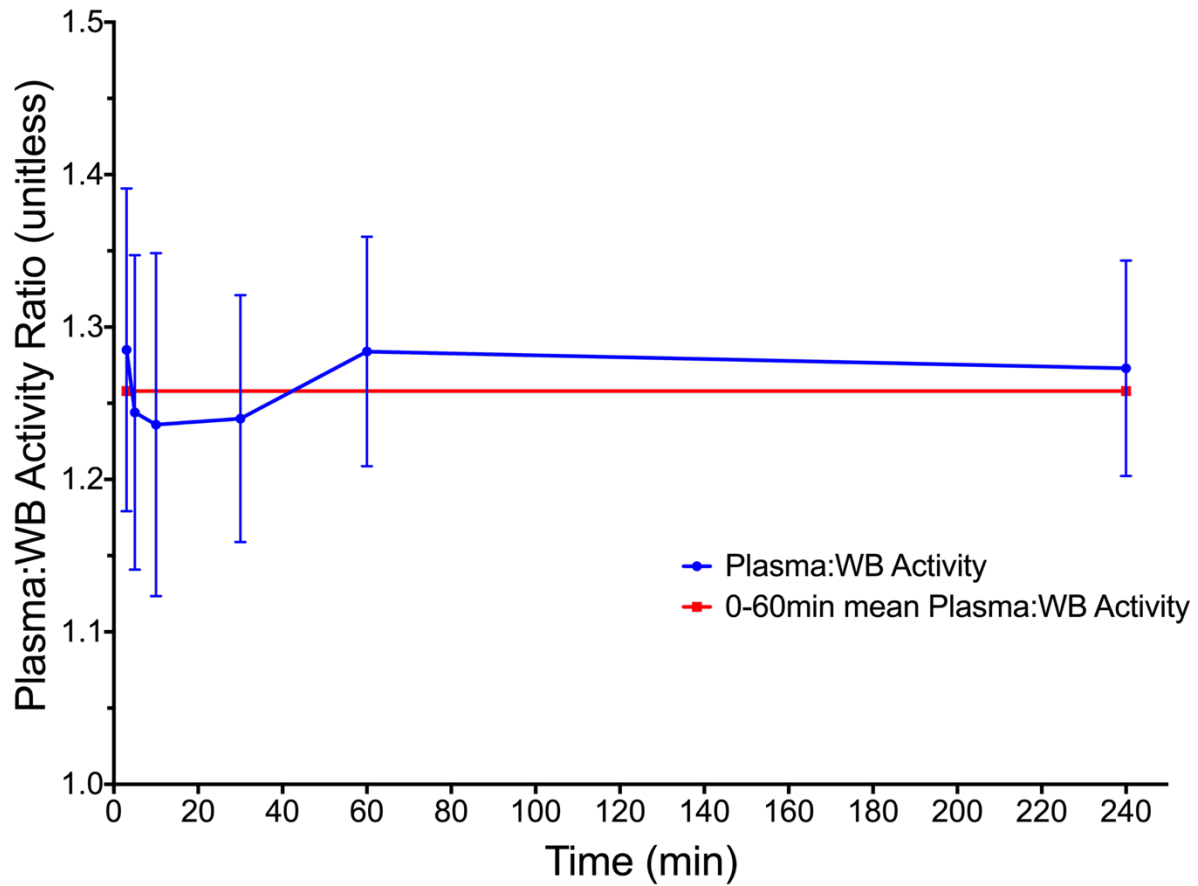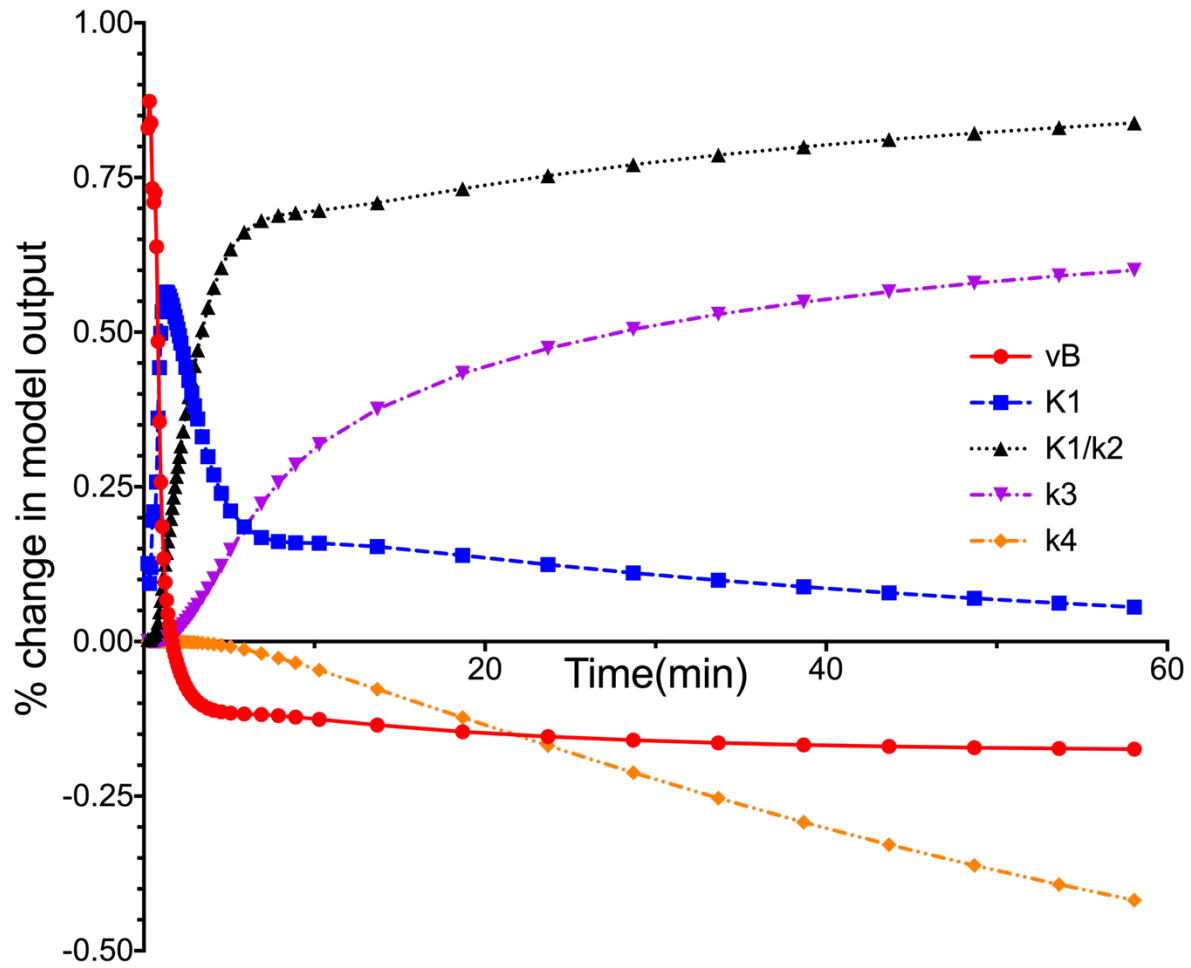
SUPPLEMENTAL FIGURES:
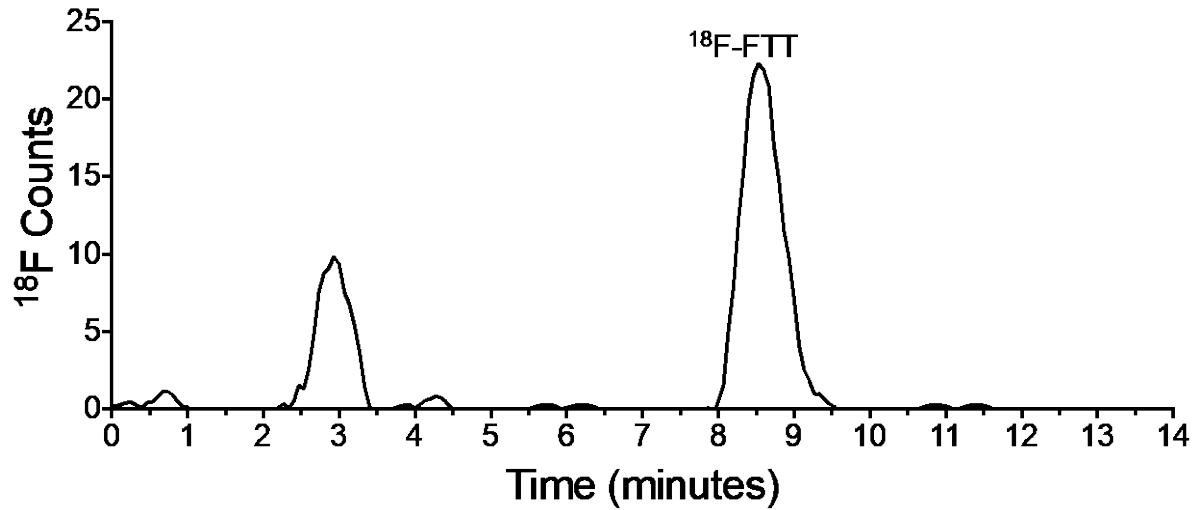
Supplemental Figure 1: Representative HPLC radiochromatogram from a 30 minute post-injection blood sample. Major metabolites were eluted at ~3 minutes, ^{18}F-FTT parent was eluted at ~8-9 minutes.
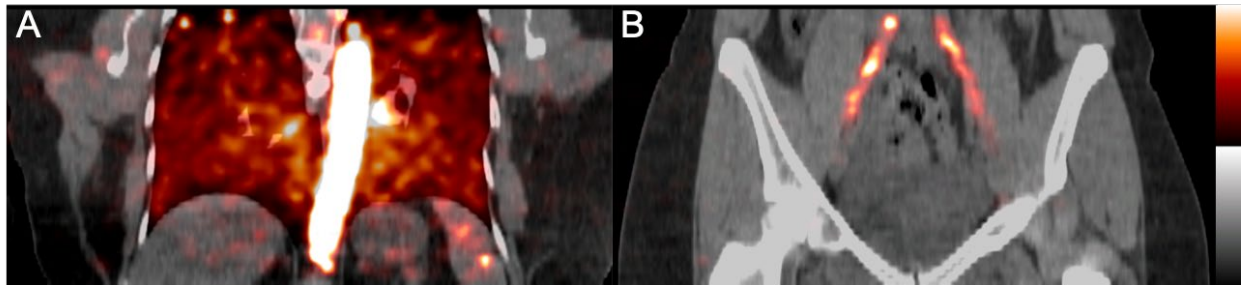

Supplemental Figure 2: Image blood pools in fused PET/CT images acquired at 30-35s post-injection of ^{18}F-FTT. Descending aorta in panel A and iliac artery in panel B VOIs were used for image derived input functions. PET images are scaled from 0-20 g/mL, CT images scaled from -160 to +240 HU.

Supplemental Figure 3: Plasma to whole blood activity ratio for ^{18}F-FTT for 16 patients with venous blood sampling. Data from 240 minutes post-injection was excluded from population average data due to low signal. Values are mean ± standard deviation. Average activity ratio from 0-60 minutes is plotted in red, and was used for correcting blood input functions in kinetic modeling.

Supplemental Figure 4: Parameter sensitivity curves for two tissue compartment model of tumor SUV_{peak} using a population average time activity curve and blood input function.
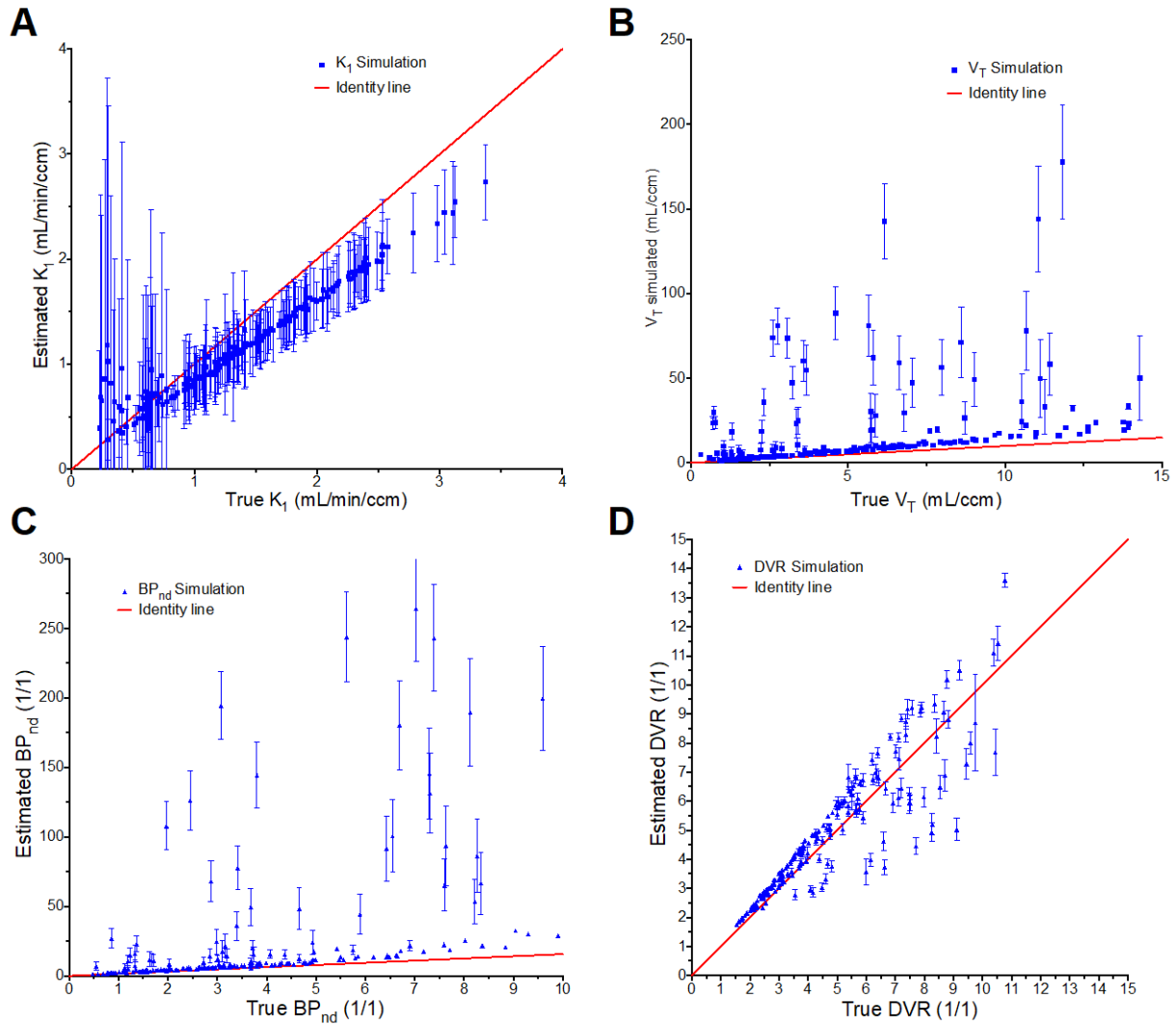
Supplemental Figure 5: Bias and precision plots of two-tissue compartment model K_1 in A, V_T in B, and nondisplaceable binding potential ($BP_{nd} = k_3/k_4$) in C. Logan reference tissue DVR in D with standard error of the mean error bars (n=200).

SUPPLEMENTAL TABLES:

Supplemental Table 1: 2 tissue compartment model fitting parameters

Model Parameter	Initial	Lower Bound	Upper bound
vB (1/1)	0.04	0.01	0.40
K_1 (mL/ccm/min)	1.50	0.0001	10
K_1/k_2 (mL/ccm)	1.10	0.0001	20
k_3 (1/min)	0.10	0.0001	1
k_4 (1/min)	0.02	0.0001	1

Supplemental Table 2: Parp-1 tissue assays and 55-60 minute PET SUVs.

Patient ID	PARP-1 immunofluorescence (Relative Fluorescence Units)	Mean Tumor Diameter (cm)	SUV_{max} (g/mL)	SUV_{peak} (g/mL)	PVC SUV_{max} (g/mL)	PVC SUV_{peak} (g/mL)
823234-02	42.7	3.10	4.06	3.26	4.34	3.45
823234-04	40.1	3.55	5.39	4.41	5.82	4.73
823234-07	59.2	2.3	8.78	7.13	9.66	7.81
823234-09	26.8	3.01	3.24	2.41	3.48	2.56
823234-10		6.15	4.15	3.65	4.40	3.84
823234-11	25.4	2.60	2.40	1.68	2.53	1.72
823234-12	22.2	2.90	4.43	3.81	4.76	4.07
823234-13	34.3	9.25	2.16	1.89	2.23	1.93
823234-15		6.55	4.81	3.92	5.15	4.16
823234-18		1.85	2.31	1.90	2.28	1.78
Mean	35.8	4.13	4.17	3.41	4.47	3.61
Standard Deviation	12.8	2.39	1.96	1.63	2.21	1.84
Median	34.3	3.05	4.11	3.46	4.37	3.65
Maximum	59.2	9.25	8.78	7.13	9.66	7.81
Minimum	22.2	1.85	2.16	1.68	2.23	1.72